Paper

ESTIMATES OF ABSORPTION OF RADIOFREQUENCY RADIATION BY THE EMBRYO AND FETUS DURING PREGNANCY

A. H. J. Fleming and K. H. Joyner*

Abstract—**This paper reports that the specific absorption rate induced in the embryo or fetus can exceed that recommended for the general public when the mother is exposed to radiofrequency radiation at the occupational limits. This result applies to two-tiered radiofrequency radiation standards where a factor of 5 differentiates occupational and nonoccupational exposure limits. Using simple axisymmetric geometries for the pregnant worker, and assuming plane wave exposures, a finite element method provides estimates of prenatal exposure. Various layered shapes are used to model skin, fat, uterus, blood, embryonic, and fetal tissues. Applying current exposure limits given by IRPA, ANSI, and SAA, the results indicate that overexposures to the embryo or fetus can occur from early pregnancy at 80–100 MHz, and in late pregnancy across the range 300–1500 MHz.**

Health Phys. 63(2):149–159; 1992

Key words: radiofrequency; pregnancy; radiation, nonionizing; exposure, prenatal

INTRODUCTION

IN GENERAL, standards for limiting human exposure to radiofrequency radiation (RFR) are two-tiered. The International Nonionizing Radiation Committee of the International Radiation Protection Association (INIRC-IRPA 1988), and other national standards-setting authorities [e.g., Standards Association of Australia (SAA) 1990], differentiate between occupational and nonoccupational (general public) exposure.

Recently, the American National Standards Institute (ANSI) (ANSI 1990) incorporated limits for controlled and uncontrolled environments.† Application of such standards would normally be straightforward. The situation becomes complicated, however, if a pregnant worker is exposed to occupational levels. What level of RFR is the developing embryo or fetus exposed to in this situation? Legal opinion suggests that the unborn child should be treated as a member of the general community and should not be exposed above the nonoccupational limits. Such protective care has already been implemented in other hazardous industries (International Labour Organization 1987). Since RFR can penetrate the body, research is needed to determine whether the RFR workplace is suitable for the pregnant employee (Hocking 1988).

With reference to the IRPA, ANSI, and SAA limits shown in Fig. 1, the question of compliance with these standards arises. Referring to Fig. 2a, mother and fetus are being exposed to an incident plane wave of power

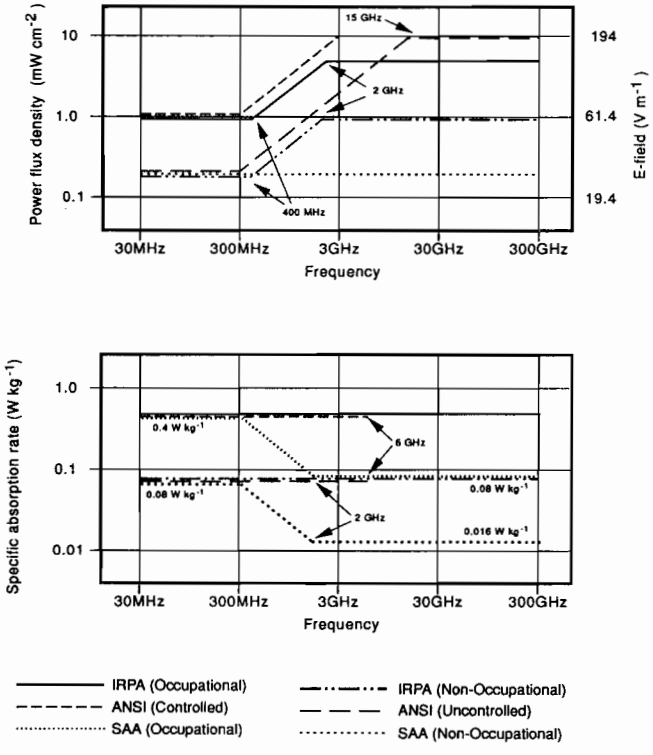

Fig. 1. IRPA, ANSI, and SAA occupational and nonoccupational incident power density limits above 30 MHz (top); IRPA, ANSI, and SAA occupational and nonoccupational SAR limits above 30 MHz (bottom).

* Telecom Australia Research Laboratories, 770 Blackburn Road, Clayton South 3168, Australia.

† In this report, two-tiered limits will be referred to as occupational and nonoccupational. In the case of the ANSI limits, controlled and uncontrolled environments is to be understood.

(*Manuscript received* 19 *June* 1991; *revised manuscript received* 14 *February* 1992, *accepted* 25 *February* 1992)
0017-9078/92/$3.00/0

density 1 mW cm^{-2} (61.4 V m^{-1}); the IRPA, ANSI, and SAA occupational limit in the frequency range 30–300 MHz. For compliance with the corresponding non-occupational limits, the developing fetus must not be exposed to a specific absorption rate (SAR) above 0.08 W kg^{-1} averaged over the fetal body.‡

In general, there are two frequency regions across the RFR spectrum where enhanced exposure of the embryo or fetus can occur, namely at whole-body resonance (80–100 MHz) in early pregnancy and a partial-body resonance in the microwave region during late pregnancy. This paper details a numerical assessment of these two effects and includes an investigation into body shape.

METHOD

To numerically estimate the SAR at the site of the embryo and fetus, certain pregnancy parameters need to be defined. Figs. 3a and b show the anatomical changes that occur between early and late pregnancy. Fig. 3a shows that in early pregnancy at the embryonic site, the SAR can be estimated by examining a small volume near the mother's body center. Fig. 3b shows that in late pregnancy, the whole-body averaged SAR of the fetus can be estimated by examining the internal fields as a function of depth below the surface of the mother's abdomen.

Geometric and dielectric parameters of pregnancy

Due to the size of the embryo in early pregnancy, the mother's size and shape may be approximated to be the same as if she were not pregnant. In later pregnancy, as the fetus develops, the spatial parameters become more difficult to define, partly due to changes in fetal shape and position that occur frequently and become a significant factor to be accounted for in any numerical model. Three important geometric parameters can be used, however, in a simple model of late pregnancy: the depth in tissue of the fetus, the fetal size, and the curvature of the mother's abdomen.

Direct measurements taken from a cross-sectioned cadaver of a mother and fetus at full term, located in the Department of Anatomy at the University of Melbourne, showed that the fetus was located approximately 19–21 mm beneath the mother's skin. Ultrasound data compare closely with this depth (Schams and Bretscher 1975). The size of the fetus was also taken from the cross-sections and from data in the literature (Blechschmidt 1961) in order to estimate the average SAR over the entire fetus, not just the nearest exposure. At full term, the estimated fetal length was 30–32 cm, the width was 12–16 cm, and the cranial diameter was 12–14 cm. The radius of the mother's abdominal curvature at full term was estimated, directly

‡ For the sake of clarity, discussion regarding differences between the breakpoints at which the ramps occur in both the IRPA and ANSI standards is left until the results of the investigation are discussed.

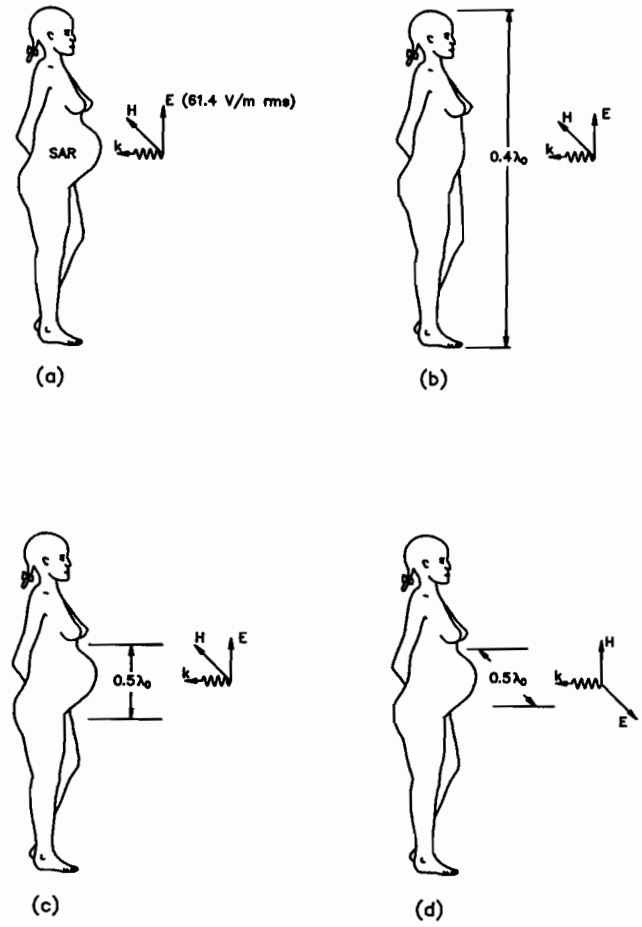

Fig. 2. (a) Basic problem: estimate the energy deposition at fetal site. (b) UHF whole-body resonance. (c) Microwave partial-body resonance; vertical polarization. (d) Microwave partial-body resonance; horizontal polarization.

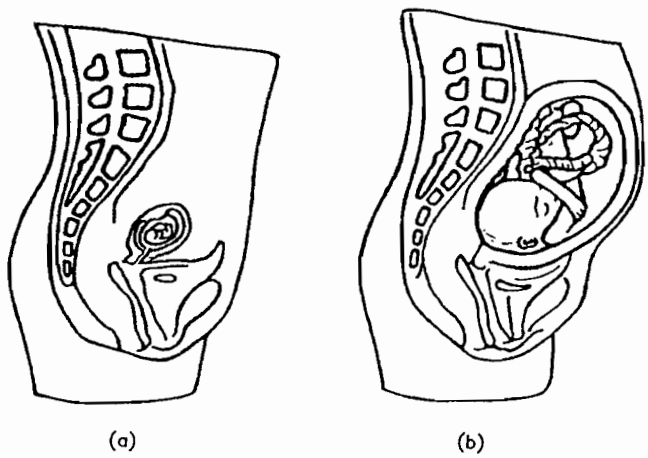

Fig. 3. Location and size of unborn child. (a) Early pregnancy. (b) Late pregnancy.

from anatomical drawings and photographs, to be 13–16 cm while the approximately spherical region subtended a total conic angle of 120° in the broadside direction (Fig. 2a). Smaller curvatures appear possible for brief periods when the fetus pushes against the uterine wall causing protrusions.

Information regarding the dielectric properties of the various biological tissues over a wide range of RFR frequencies was taken from the Radiofrequency Radiation Dosimetry Handbooks (Johnson et al. 1976; Durney et al. 1978; Durney et al. 1980; and Durney et al. 1986). Curves of best fit of experimental dielectric measurements provide succinct programmable information. In published numerical estimates of RFR absorption, however, a range of dielectric models has been used and thus the resulting internal absorption levels also vary (see Table 1).

Whole-body resonance

At frequencies between 75–100 MHz, depending upon the size of the mother, whole-body resonance in free space occurs when the female body height is approximately 0.4 λ_0, where λ_0 is the free-space wavelength, as illustrated in Fig. 2b. In this case, body size and shape affect the SAR levels at the site of the embryo and the fetus.

It is known from homogeneous whole-body spheroidal modeling (Durney et al. 1978) that the thinness ratio (height:width) of the body affects the whole-body average SAR. Thus the average SAR of a small female (height 1.45 m, weight 43.09 kg) is larger than that of an average female (1.61 m, 61.14 kg), which in turn is larger than that produced in a large female (1.73 m, 88.45 kg).

An assessment is required as to how whole-body resonance is affected by the shape and size of the fully-developed fetus in late pregnancy. Comparing the fields inside two spheroids of the same dielectric composition and height but of different widths as shown in Figs. 4a and b, the vertical E-field inside the wider spheroid will be the lower (Durney et al. 1986, p. 5.29). A comparison can then be made with late pregnancy, modeled as shown in Fig. 4c, by a combined shape of the thin spheroid, Fig. 4a, and a sphere of diameter equal to the width of the wider spheroid, Fig. 4b.

Partial-body resonance due to late pregnancy

A second mechanism for enhanced energy absorption to the fetus occurs in the microwave or ultrahigh frequency portion of the spectrum. This effect depends on the curvature and size of the mother and fetus during late pregnancy. At full term, the combined shape of mother and fetus is partially rounded and can resonate like a large dielectric sphere producing a subdued hot-spot effect (Shapiro et al. 1971; Kritikos and Schwan 1972) as illustrated in Figs. 2 c and d, where the incident field may now be either vertically or horizontally polarized. In both cases, the protuberant, rounded portion of the mother's body is approximately 0.4–0.5 λ_0 in diameter. Because RFR absorption by the fetus in these cases occurs primarily in the first few centimeters below the mother's skin surface (see Fig. 5), and because the fetus can change position to be either lying in a vertical or horizontal position, both polarizations need consideration. Using spherical models for both, of course, produces identical results.

An assessment is required to determine how the rest of the mother's body—her upper torso, head, and legs—alter microwave absorption during late pregnancy. Given that the effect is that of a subdued hot spot, any change in SAR levels at the fetal site due to the rest of the body is likely to be small, as discussed later.

Numerical method

Prior to outlining details and results of the finite element method used to provide estimates of absorption during pregnancy, the need for such computations requires consideration. First, no direct dosimetry data for either the developing embryo or fetus is currently available.

As mentioned, absorption characteristics are required at anatomical locations in early pregnancy near the mother's body center and in late pregnancy at depths below the uterine wall. Some indicative numerical information is available during early pregnancy. Averaged results over large neighboring regions close to the embryonic site, or at least its equivalent in male models, have been published. These results were not at 90 MHz, the resonant frequency for a small female (height 1.45 m, weight 43.09 kg). However, no data specifically at the embryonic site or for a small female are known to the authors. Again, during late pregnancy, no data, even indicative, are currently available.

Moreover, from the published literature there exists a range of results indicating SAR levels of 0.4 W kg^{-1} down to about 0.1 W kg^{-1} (see Table 1). This range was considered to be a function of the numerical models employed and their simplicity, for example, whether homogeneous or not. A more-detailed dielectric model was considered necessary in refining the results quantitatively. To further explain this range of results, frequencies not exactly at resonance can produce a significant lowering of internal SAR levels. An examination across the suspected resonant frequency bands, especially at whole-body resonance, was thus desired.

A finite-element method based upon a formulation of Maxwell's equations for the solution of isotropic, inhomogeneous bodies of revolution involving two coupled azimuthal potentials (Morgan and Mei 1979) was used to numerically estimate absorption levels within the female body. The major advantage of the coupled azimuthal potentials (CAPs) formulation is that only two variables are required to be determined at each field point, resulting in major cost savings over other

Table 1. Comparison of estimates of SAR at embryonic site.

Model	Dielectric constants $\epsilon'_r - j\,\epsilon''_r$	Frequency (MHz)	SAR (W kg^{-1})
Durney et al. (1978) pp. 78–83 EBCM/empirical Homogenous spheroid small woman	Durney et al. (1978), p. 61 46 − j 112[a]	90	0.26 whole body average
Durney et al. (1986) pp. 6.2–6.8 EBCM	Durney et al. (1986), pp. 4.39–4.70		
Homogenous spheroid average woman	49 − j 119[a]	80	0.23 average whole body
Homogenous spheroid large woman	50 − j 127[a]	75	0.20 average whole body
Homogenous spheroid average man	50 − j 127[a]	75	0.26 average whole body
Hagmann et al. (1979) Moment method Homogenous block model average man	2/3 muscle	80	0.40 at equivalent embryonic site
Chen and Guru (1977) Tensor integral equation method Homogenous block model average man	80 − j 188.7	80	0.25 at equivalent embryonic site
ABSBOR Finite element method Homogenous spheroid small woman	Durney et al. (1978), p. 61 46 − j 112[a]	90	0.26 at embryonic site xy ave ± 3 cm ($z = 0$)
ABSBOR Finite element method Layered spheroid small woman	-skin 48.0 − j 160.0 -fat 6.0 − j 20.0 -muscle and blood 76.1 ≥ j 140.2	90	0.25 at embryonic site xy ave ± 3 cm ($z = 0$)
Sullivan et al. (1988) Finite difference time domain method Homogenous model average man	71.7 − j 159.8	100	0.10 averaged at half height
ABSBOR Finite element method Homogenous spheroid small woman	71.7 − j 159.8	100	0.09 at embryonic site xy ave ± 3 cm ($z = 0$)
Sullivan et al. (1988) Finite difference time domain method Inhomogenous model average man		100	0.15 averaged at half height
ABSBOR Finite element method Layered spheroid small woman	-skin 48.0 − j 144.0 -fat 6.0 − j 18.0 -muscle, and blood 75.3 − j 127.7	100	0.19 at embryonic site xy ave ± 3 cm ($z = 0$)

[a]Dielectric values estimated from reference.

differential formulations. An outline of the method used is presented in the Appendix.

The resulting numerical procedure for the analysis of the internal absorption characteristics of layered bodies of revolution, termed ABSBOR, was initially applied to a series of spherical geometries to obtain a

basic validation. These tests were performed using dielectric constants and object sizes appropriate for the suspected effect at microwave frequencies during late pregnancy. Available for comparison was a procedure based on the Mie series solution, called SCAT2, for computing the absorption characteristics of layered spherical objects (Neuder 1979). The results of this first round of tests were most convincing and where absorption levels were significant, errors were small between the results given by ABSBOR and SCAT2 (Fig. 6).

A second series of tests designed to investigate more-elongated objects was then conducted. ABSBOR results were compared with those obtained by Barber (1977a) who used the Extended Boundary Condition Method (EBCM) to calculate the internal fields of small spheroids. Although there appeared to be some dependence on how the mesh was discretized, reasonable results were obtained by ABSBOR when careful mesh and modal parameter selection was performed.

A final test using whole-body averaged SAR data for a spheroidal model of a sitting rhesus monkey at 300 MHz was performed (Durney et al. 1978, p. 81). Results for SAR along the x and y axes were found to agree with expected whole-body averaged results, while those along the z-axis were now found to be in large error due to the numerical boundary conditions along the z-axis (see the Appendix). Trials for thinner objects, appropriate for human whole-body modeling, were consequently performed using the x-axis and y-axis results, and not the z-axis.

The numerical mesh parameters for the present application were chosen by careful selection during this trial period. The number of divisions in the elevational angle (θ, as measured from the z-axis) was 35–75, while the radial grid density in terms of radial nodes per wavelength was, in all cases, 25–35. The modal parameters were chosen on a case-by-case basis depending upon the dielectric constants and electrical sizes of the objects involved. In general, the first four (0–3) azimuthal modes and up to 14 radial modes were used.

The CAP calculations for the whole-body modeling involved large meshes and lengthy calculations. Previous attempts have been made to overcome these computational bottlenecks by combining the EBCM and the CAP formulations into a hybrid method for analyzing elongated structures (Morgan et al. 1984). Unfortunately, the associated series of modal solutions were not monotonically convergent for large eccentricities (Morgan 1990). The present computations circumvented these difficulties by utilizing an out-of-core block inversion technique. Nevertheless, most computations were very long running. The finite element mesh size and, hence, the computational effort are related to the thinness ratio in that a wider submatrix size is required for larger ratios. For this reason, and because it absorbed the highest SAR levels (Durney et al. 1978, 1986), subsequent numerical effort centered on models of a small mother and her embryo or fetus.

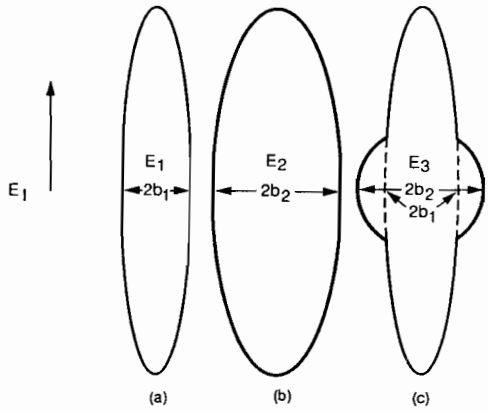

Fig. 4. Spheroidal models to investigate the effect of the anatomical shape of late pregnancy on whole-body resonance. (a) Thin spheroid. (b) Wide spheroid. (c) Thin spheroid and sphere combined.

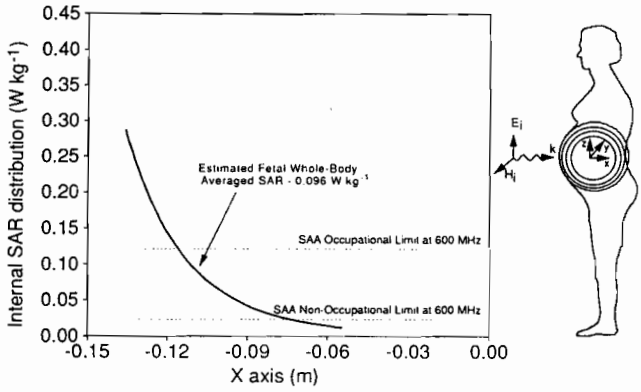

Fig. 5. SAR distribution within layered spherical models of mother and fetus.

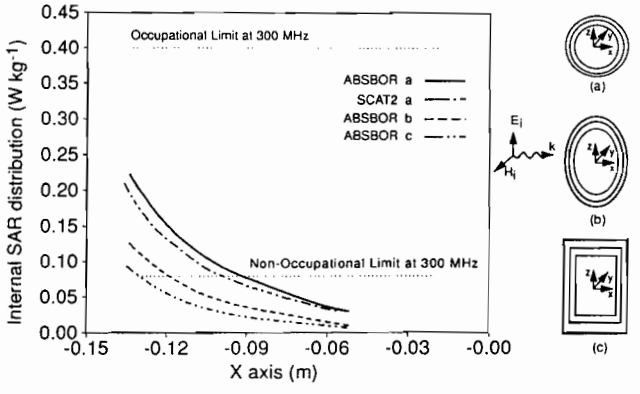

Fig. 6. SAR distribution at fetal site using different-shaped, layered models of mother and fetus.

RESULTS

Whole-body resonance

A vertically polarized plane wave of power density 1 mW cm^{-2} was assumed incident upon a number of axisymmetric finite element female models, assumed standing upright in free space. To obtain a basic validation of the numerical method at whole-body resonance, a series of tests was performed using simple dielectric models and results were compared with published data (Table 1).

First, a homogeneous spheroidal model of a small female in early pregnancy was examined at 90 MHz. The complex permittivity, 46–j112, and the dimensions of the spheroid (2a = 1.45 m, b = 0.12 m) were taken from the handbooks (Durney et al. 1978, p. 61; Johnson et al. 1976, p. 20). Figs. 7a and b show the SAR distribution of a region 3 cm about the spheroid center in the x and y directions. The SAR is fairly smooth inside this region and averages around 0.26 W kg^{-1}. This result is consistent with the whole-body average SAR results obtained using the EBCM (Barber 1977b) and published in the handbooks.

Another test now compared more-localized SAR distributions, again using a spheroidal model of a small female, but with different dielectric constants and at a different frequency. The internal SAR distribution of a homogeneous male model was obtained by Sullivan et al. (1988) using a finite difference method at 100 MHz and a complex permittivity of 71.7–j159.8 (σ = 0.889 S m^{-1}). Their SAR results were averaged across the anatomy at various heights within the body. At the height of the equivalent embryonic site, they found an averaged SAR of approximately 0.10 W kg^{-1}. Using ABSBOR, the results (Figs. 7a and b) were averaged ±3 cm in the x–y plane and found to be 0.09 W kg^{-1}.

A second series of tests was now conducted using anatomically more-realistic models. An inhomogeneously layered small female spheroidal model was tested, this time for a range of frequencies, 80–100 MHz, using a step size of 5 MHz. Frequency-dependent dielectric parameters were chosen to model a 6-mm layer of skin, a 10-mm layer of fat, and a homogeneous interior region of blood and muscle. Resonance within a region ± 3 cm along the x and y axes (i.e, the embryonic site) occurred as expected at 90 MHz (Figs. 7a and b). The estimated averaged SAR at the embryonic site was 0.25 W kg^{-1} at 90 MHz and 0.20 W kg^{-1} at 80 MHz.

Corresponding to their homogeneous model, Sullivan et al. (1988) also tested an inhomogeneous male model, at 100 MHz, using dielectric constants for various tissues by referencing a series of anatomical cross-sections. At the height of the equivalent embryonic site, their averaged SAR result, 0.15 W kg^{-1}, was higher than that of their homogeneous male model. Using ABSBOR, the averaged result, 0.19 W kg^{-1}, was also higher than the corresponding homogeneous model results.

A final test at whole-body resonance investigated the effect of late pregnancy upon whole-body resonance as illustrated by Figs. 4a, b, and c. An inhomogeneous-layered spheroidal model of a small female in late pregnancy was modeled as a spheroid (2a = 1.45 m, b_1 = 0.12 m) and a protruding sphere (b_2 = 0.15 m) as shown in Fig. 4c. Similarly, a wider spheroid, as shown in Fig. 4b, with the same radius (0.15 m) as the model of the small female in late pregnancy was also modeled. Both models were examined across the range 80–100 MHz using 5-MHz steps, which was found to occur at around 90 MHz. Results for both models at 90 MHz are compared with those of the small female in early pregnancy, Figs. 8a and b, indicating that the small spheroid is the worst case in that it produces the highest internal SAR distribution at the embryonic site. The larger spheroid produces a lower SAR distribution, with the small spheroid-plus-sphere producing the lowest SARs.

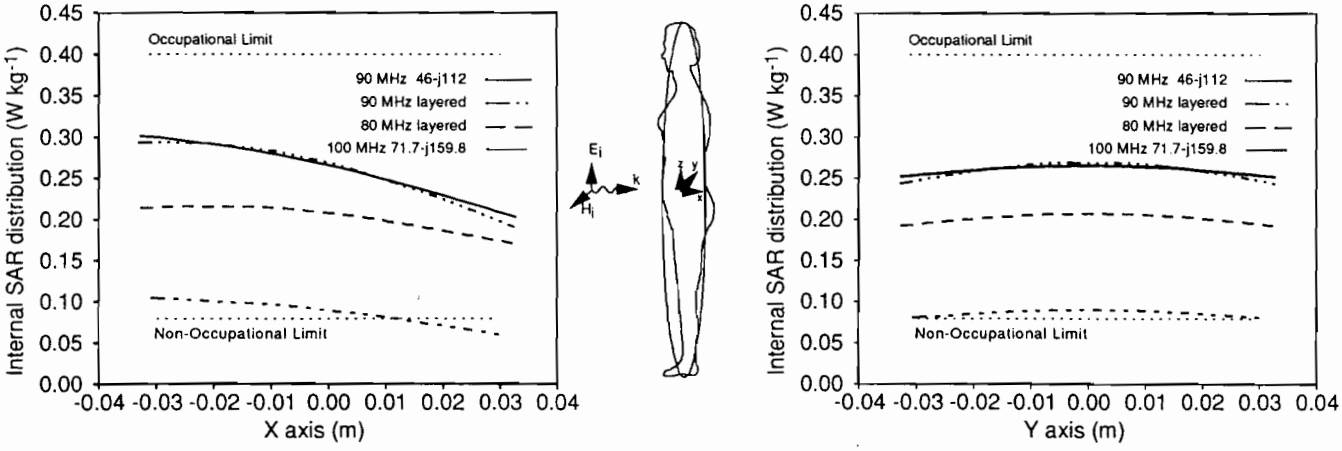

Fig. 7. (a) SAR distribution at embryonic site along x-axis using spheroidal models of small mother at and near resonance. (b) SAR distribution at embryonic site along y-axis using spheroidal models of small mother at and near resonance.

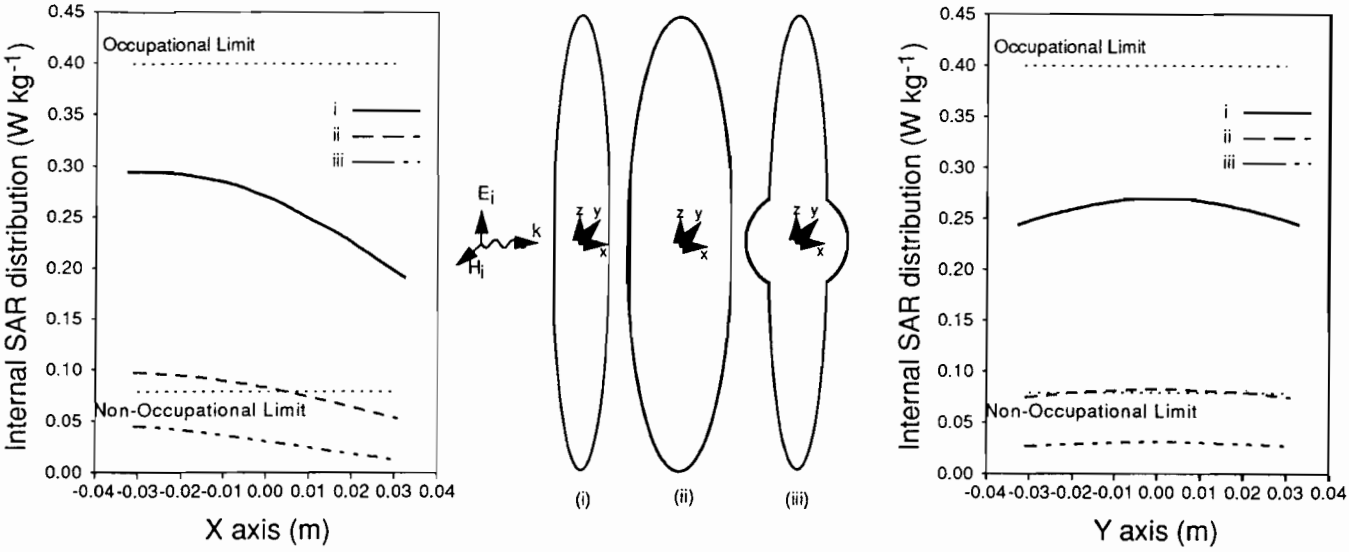

Fig. 8. (Left) SAR distribution at embryonic site along x-axis using different-shaped models of small mother at resonance. (Right) SAR distribution at embryonic site along y-axis using different-shaped models of small mother at resonance.

Table 2. Comparison of estimates of SAR at fetal site.

Model	Frequency (MHz)	SAR (W kg^{-1}) at depths below the skin		
		2.0 cm	5 cm	10 cm
Layered sphere	300	0.17	0.08	0.030
Layered sphere	600	0.22	0.07	0.012
Layered sphere	900	0.22	0.05	0.006
Layered sphere	1200	0.16	0.03	0.002
Layered sphere	1500	0.10	0.02	0.001
Layered spheroid	300	0.11	0.05	0.009
Layered cylinder	300	0.08	0.03	0.006

While attempting to verify this result, the authors consider that this seemingly anomalous effect may be due to differences in the local curvature radius of the mother's body overlying the embryonic site for the three cases. The thin spheroid has the largest curvature radius, the wide spheroid is intermediate, and the curvature of the sphere is smallest, apparently being more able than the wide spheroid to interfere with the whole-body resonance caused by the spheroidal shape alone.

Microwave partial-body resonance

The effect of late pregnancy at microwave frequencies was now investigated using a number of different models, assuming an incident plane wave of 1 mW cm^{-2}. All results were later scaled to account for the ramps that occur with both the IRPA and ANSI standards (Fig. 1).

The electrical size and associated computational effort necessary for examining the whole body above about 300 MHz prevent use of a model involving the complete body, top to bottom. Instead, the localized region including the fetus and surrounding tissues must suffice for this case. In the first instance, the partially hemispherical geometry of late pregnancy can be examined using a spherical model, the assumption being that the fetal region will be dominated by localized tissue effects.

Initially, the multilayered Mie series program, SCAT2, provided results across a sweep of frequencies from 300–1500 MHz. The spherical models of mother and fetus included layers of skin, fat, uterus (dielectric constant chosen as equivalent to muscle), and a homogeneous interior of blood and muscle representing the fetus, placenta, and amniotic fluid (since these tissues are not dissimilar from an electromagnetic point of view). Sphere sizes ranging from 14–20-cm radius were checked, representing a wide variation across pregnancies. Layer thicknesses used were 4 mm for skin, 10 mm for fat, and 6 mm for the uterus.

The internal SAR in the direction of propagation at 600 MHz is shown in Fig. 5 for a 15-cm-radius sphere. At this frequency, the maximum fetal exposure, 0.22 W kg^{-1}, occurred at a depth of 20 mm (the inside of the uterine wall). At this depth in tissue, the developing fetus will only have one side of its body absorbing at this level.

Table 2 shows how the local SAR varies with depth in tissue. A 15-point grid was used to estimate the whole-body averaged exposure over the entire fetal

body. The grid's points within the spherical volume were chosen to correspond to points within the fetus as it lay in the fetal position, head up and curled inside the uterus, with its face pointing away from the mother's abdomen. The points were about 3–6 cm apart in all directions (x, y, and z) and spanned a portion of the inner layer of the spherical model. In this way, the whole-body averaged SAR was estimated to be 0.096 W kg^{-1} at 600 MHz. Similar results were found at frequencies ranging from 300 MHz up to 1500 MHz, as shown in Table 2.

Tables 3, 4, and 5 show the estimated whole-body averaged fetal SARs when applying the IRPA, ANSI, and SAA occupational limits at each frequency. While these results were obtained using a 15-cm sphere, it should be noted that smaller spherical models produce larger internal fields. Photographic data show that local curvatures of radius can be 13.5 cm and perhaps lower. Overlying tissues can be thinner than 2 cm, even as thin as 1 cm (Carson 1988), further increasing the possible fetal exposure.

ABSBOR was used to test other related geometries such as small spheroids and cylinders, to see what effect the rest of the body or differing local curvatures might have. These tests showed that the curvature due to a layered spherical model produced the highest internal

Table 3. Comparison of estimated fetal exposures at microwave frequencies with IRPA RFR exposure guidelines.

Frequency (MHz)	Occupational power density (mW cm^{-2})	Occupational SAR limit (W kg^{-1})	Nonoccupational SAR limit (W kg^{-1})	Estimated fetal exposure (W kg^{-1})
300	1.00	0.4	0.08	0.094
600	1.50	0.4	0.08	0.144
900	2.25	0.4	0.08	0.203
1200	3.00	0.4	0.08	0.202
1500	3.75	0.4	0.08	0.158

Table 4. Comparison of estimated fetal exposures at microwave frequencies with ANSI RFR exposure limits.

Frequency (MHz)	Controlled environment power density (mW cm^{-2})	Controlled environment SAR limit (W kg^{-1})	Uncontrolled environment SAR limit (W kg^{-1})	Estimated fetal exposure (W kg^{-1})
300	1.0	0.4	0.08	0.094
600	2.0	0.4	0.08	0.192
900	3.0	0.4	0.08	0.271
1200	4.0	0.4	0.08	0.269
1500	5.0	0.4	0.08	0.211

Table 5. Comparison of estimated fetal exposures at microwave frequencies with SAA RFR exposure limits.

Frequency (MHz)	Occupational power density (mW cm^{-2})	Occupational SAR limit (W kg^{-1})	Nonoccupational SAR limit (W kg^{-1})	Estimated fetal exposure (W kg^{-1})
300	1.0	0.400	0.080	0.094
600	1.0	0.116	0.023	0.096
900	1.0	0.100	0.020	0.090
1200	1.0	0.092	0.018	0.067
1500	1.0	0.086	0.017	0.042

SAR distribution. At 300 MHz, a small layered spheroid of similar radius to the layered spheres (with a height-to-width ratio of 1.5:1) and a cylinder of similar dimensions were investigated. The results, shown in Fig. 6 and listed in Table 2, suggest that actual fetal exposures during late pregnancy will be somewhat lower than the results obtained using spherical-layered models.

CONCLUSIONS

Numerical estimates indicate that in early pregnancy, due to whole-body resonance between 80–100 MHz, the embryo may be exposed to SAR levels above recommended general population limits for IRPA, ANSI, and SAA if the mother is exposed to occupational limits. The results also indicate that absorption levels at whole-body resonance are affected by body shape and that the shape of early pregnancy produces the most enhanced internal fields. Body shape due to later stages of pregnancy reduces this level of absorption.

As to the microwave effect in late pregnancy, estimates across a range of frequencies from about 300–1500 MHz indicate that similar exposures above general population limits for IRPA, ANSI, and SAA are possible. This partial-body resonance effect due to the body shape of late pregnancy requires further quantitative definition as the spherical model is only a first-order representation of the actual case. The electrical size of this problem precluded a complete solution using ABSBOR. The testing of shapes other than layered spheres indicates that the actual exposure levels at the fetal site in late pregnancy will be somewhat lower when body shape effects are taken into account.

Further research in a number of areas is required such as near-field effects and the presence of various types of ground planes. It is hoped that recent developments in the CAP formulation can be used to investigate non-axisymmetric finite element models of pregnancy.

Given that legal opinion suggests that the unborn child be treated as a member of the general community and not be exposed above the nonoccupational limits, standards-setting authorities should consider the incorporation of protective care of mother and child into RFR exposure limits.

Acknowledgements—The authors would like to thank V. Lubinas, B. Hocking, J. Lumely, R. Thompson, V. Gusman, A. Mitchell, M. Phipps, A. Norrish, and M. Rogers for their help and assistance during the course of this work. Professor M. Morgan kindly availed the authors of his computer program upon which the code ABSBOR was based. The assistance of the Department of Anatomy, University of Melbourne, is gratefully acknowledged; fetal measurements were conducted at the museum within the Department. Permission to publish by the Executive General Manager, Telecom Australia Research Laboratories is hereby acknowledged.

REFERENCES

Amerian National Standards Institute, Inc. American national standard safety levels with respect to human exposure to radio-frequency electromagnetic fields, 3 kHz to 300 GHz. New York: ANSI; ANSI C95.1-1991; 1990.

Barber, P. W. Electromagnetic power deposition in prolate spheroid models of man and animals at resonance. IEEE Trans. Biomed. Eng. BME-24:513–521; 1977a.

Barber, P. W. Resonance electromagnetic absorption by nonspherical dielectric objects. IEEE Trans. Microwave Theory Tech. MTT-25:373–381; 1977b.

Blechschmidt, E. The stages of human development before birth, an introduction to human embryology. Philadelphia, PA: W. B. Saunders; 1961.

Carson, P. L. Medical ultrasound fields and exposure measurements. In: Proceedings of the 22nd annual meeting of the National Council on Radiation Protection and Measurements. Bethesda, MD: NCRP; 1988:287–307.

Chang, H.; Mei, K. K. Scattering of EM waves by buried or partly buried body of revolution. In: Proceedings of the IEEE symposium on antennas and propagation; Los Angeles: IEEE; 1981:653–656.

Chen, K. M.; Guru, B. S. Focal hyperthermia as induced by RF radiation of simulacra with embedded tumors and as induced by EM fields in a model of a human body. Radio Science 12(6S):27–37; 1977.

Durney, C. H.; Iskander, M. F.; Massoudi, H.; Allen, S. J.; Mitchell, J. C. Radiofrequency radiation dosimetry handbook. 3rd ed. Brooks Air Force Base, TX: USAF School of Aerospace Medicine; SAM-TR-80–32; 1980.

Durney, C. H.; Johnson, C. C.; Barber, P. W.; Massoudi, H.; Iskander, M. F.; Lords, J. L.; Ryser, D. K.; Allen, S. J.; Mitchell, J. C. Radiofrequency radiation dosimetry handbook. 2nd ed. Brooks Air Force Base, TX: USAF School of Aerospace Medicine; SAM-TR-78–22; 1978.

Durney, C. H.; Massoudi, H.; Iskander, M. F. Radiofrequency radiation dosimetry handbook. 4th ed. Brooks Air Force Base, TX: USAF School of Aerospace Medicine; SAM-TR-85–73; 1986.

Fleming, A. H. J. A finite element method for composite scatterers. In: Morgan, M. A., ed. Finite element and finite difference methods in electromagnetic scattering, progress in electromagnetic research. Vol. 2; New York: Elsevier; 1990.

Hagmann, M. J.; Ghandi, O. P.; Durney, C. H. Numerical calculation of electromagnetic energy deposition for a realistic model of man. IEEE Trans. Microwave Theory Tech. MTT-27:804–809; 1979.

Hocking, B. Occupational health—a physician's viewpoint as exemplified by radiofrequency radiation concerns. In: Repacholi, M. H., ed. Non-ionizing radiations—physical characteristics, biological effects and health hazard assessment, proceedings of the internal non-ionizing radiation workshop. Melbourne: IRPA; 1988:422–423.

International Labour Organization. Radiation protection of workers (ionizing radiations). Geneva: International Labor Office; 1987.

International Non-Ionizing Radiation Committee of the International Radiation Protection Association (INIRC-IRPA). Guideline on limits of exposure to radio-frequency electromagnetic fields in the frequency range from 100 kHz to 300 GHz . Health Phys. 54:115–123; 1988.

Johnson, C. C.; Durney, C. H.; Barber, P. W.; Massoudi, H.; Allen, S. J.; Mitchell, J. C. Radiofrequency radiation do-

simetry handbook. Brooks Air Force Base, TX: USAF School of Aerospace Medicine; SAM-TR-76-35; 1976.
Kritikos, K. N.; Schwan, H. P. Hot spots generated in conducting spheres by electromagnetic waves and biological implications. IEEE Trans. Biomed. Eng. BME-19:53-58; 1972.
Morgan, M. A. Finite element calculation of microwave absorption by the cranial structure. IEEE Trans. Antennas Propagat. BME-28:687-695; 1981.
Morgan, M. A. Coupled potentials for electromagnetic fields in inhomogeneous media. In: Morgan, M. A., ed. Chapter 6 of Finite element and finite difference methods in electromagnetic scattering, progress in electromagnetic research. Vol. 2: New York: Elsevier Applied Science Publishers; 1990: 211-247.
Morgan, M. A.; Chen, C. H.; Hill, S. C.; Barber, P. W. Finite element—boundary integral formulation for electromagnetic scattering. Wave Motion 6:91-103; 1984.
Morgan, M. A.; Mei, K. K. Finite element computation of scattering by inhomogeneous bodies of revolution. IEEE Trans. AP-27:203-214; 1979.
Neuder, S. M. Electromagnetic fields in biological media, Part II—The SCAT program, multilayered spheres, theory and applications. Rockville, MD: U.S. Department of Health, Education and Welfare, Bureau of Radiological Health; HEW publication (FDA) 79-8072; 1979.
Schams, H.; Bretscher, J. Ultrasonographic diagnosis in obstetrics and gynecology. New York: Springer-Verlag; 1975.
Shapiro, A. R.; Lutomirski, R. F.; Yura, H. T. Induced fields and heating within a cranial structure irradiated by an electromagnetic plane wave. IEEE Trans. Microwave Theory Tech. MTT-19:187-196; 1971.
Standards Association of Australia (SAA). Radio-frequency radiation Part 1: Maximum exposure levels—100 kHz to 300 GHz. North Sydney, Australia: Standards House; AS2772.1; 1990.
Sullivan, D. M.; Ghandi, O. P.; Taflove, A. Use of finite difference time-domain method for calculating EM absorption in man models. IEEE Trans. Biomed. Eng. BME-35:179-186; 1988.

APPENDIX
Coupled Azimuthal Potentials (CAP) Formulation

The CAP formulation has thus far been used to solve structurally complex problems involving lossy dielectrics (Morgan and Mei 1979; Morgan 1981), objects interacting with a ground plane (Chang and Mei 1981), and composites (Fleming 1990), to name a few. The objects involved have been axisymmetric, although use of Fourier analysis has allowed interactions of bodies of revolution with plane wave and generalized aperture sources to be analyzed.

For these axisymmetric objects, the inhomogeneous cross-sections are regions where both the shape and the constitutive parameters are rotationally (ϕ) invariant, $\epsilon(r,\theta) = \epsilon_0\epsilon_r(r,\theta)$; $\mu(r,\theta) = \mu_0\mu_r\ (r,\theta)$. The axisymmetric CAP formulation begins by rewriting Maxwell's time harmonic curl equations using a Fourier series for the fields in the aximuthal coordinate, ϕ, thus separating the azimuthal variable:

$$\bar{E}(R, Z, \phi) = \sum_{m=-\infty}^{\infty} \bar{e}_m(R, Z)\exp(jm\phi) \quad \text{(A1a)}$$

$$\eta_0\bar{H}(R, Z, \phi) = \sum_{m=-\infty}^{\infty} \bar{h}_m(R, Z)\exp(jm\phi). \quad \text{(A1b)}$$

After suitable algebraic manipulation of the resulting equations and substituting the modal CAP variables $\psi_{1,m}$ and $\psi_{2,m}$, the result is:

$$\Psi_{1,m} = Re_{\phi,m} \quad \text{(A2a)}$$

$$\Psi_{2,m} = Rh_{\phi,m}. \quad \text{(A2b)}$$

In terms of the azimuthal modal fields, the following system of coupled second-order partial differential equations is derived:

$$\nabla.[f_m(R\epsilon_r\nabla\Psi_{1,m} + m\hat{\phi}\times\nabla\Psi_{2,mp})] + \epsilon_r\Psi_{1,m}/R = 0 \quad \text{(A3a)}$$

$$\nabla.[f_m(R\mu_r\nabla\Psi_{2,m} - m\hat{\phi}\times\nabla\Psi_{1,m})] + \mu_r\Psi_{2,m}/R = 0, \quad \text{(A3b)}$$

where ∇, the cross-sectional gradient operator, is defined by:

$$\nabla = \hat{R}\frac{\partial}{\partial R} + \hat{Z}\frac{\partial}{\partial Z} \quad \text{(A4a)}$$

and $$f_m = [\epsilon_r(R, Z)\mu_r(R, Z)R^2 - m^2]^{-1}. \quad \text{(A4b)}$$

Using an interpolant $\hat{\psi}^*$ to approximate the fields within each element by a piecewise polynomial representation, Galerkin's method (Fleming 1990) is applied at all nodes N_I in the mesh description of the problem:

$$\sum^{N_{e(i)}} \int_{A_e} W_e|\{\bar{\Psi}_e^*\}|\,dA_e = \bar{0} \quad \text{for } i = 1, N_I, \quad \text{(A5)}$$

where $N_{e(i)}$ is a mesh-dependent function that describes the elements associated with each node of the element and W_e is a weighting function. The vertical bars indicate a nodal matrix of dimension $N_I \times N_I$, and the independent variable of integration is the area of each element A_e.

In order to use this formulation for problems involving infinite regions, the inhomogeneous finite element mesh region was coupled to the surrounding infinite exterior-free space region. This was done by using a series of spherical harmonic functions repre-

senting the plane wave applied at a semicircular contour. A moment method was now used to numerically enforce electromagnetic continuity between the two regions. An internal homogeneous core region similarly separated by a core semicircular contour was also used. In this core region, spherical harmonics were again used to obtain the fields.

For coupling with the CAP formulation, the surfaces that separate the regions can be of any shape that permit the convenient orthogonal separation of the azimuthal coordinate, ϕ, into the spectral modes, $e^{jm\phi}$. In the present application, spheres and spherical harmonics were used. In terms of these spherical harmonic functions, the modal azimuthal fields may be written in terms of the radial electric and magnetic vector potential components, $F_{r,m}$ and $A_{r,m}$:

$$E_{\phi,m} = \frac{1}{r}\frac{\partial F_{r,m}}{\partial \theta} + \frac{1}{j\mu\epsilon\, r \sin\theta}\frac{\partial^2 A_{r,m}}{\partial r \partial \phi} \quad \text{(A6a)}$$

$$H_{\phi,m} = -\frac{1}{r}\frac{\partial A_{r,m}}{\partial \theta} + \frac{1}{j\omega\mu\, r \sin\theta}\frac{\partial^2 F_{r,m}}{\partial r \partial \phi}, \quad \text{(A6b)}$$

where

$$F_{r,m} = \frac{\sqrt{\mu_r}}{k}\sum_{n=m}^{N_m} a_{mn} P_n^m(\cos\theta)\hat{B}_n(kr)\exp(jm\phi) \quad \text{(A6c)}$$

$$A_{r,m} = \frac{\sqrt{\epsilon_r}}{\eta_0 k}\sum_{n=m}^{N_m} b_{mn} P_n^m(\cos\theta)\hat{B}_n(kr)\exp(jm\phi), \quad \text{(A6d)}$$

and where the complex propagation constant $k = \omega\sqrt{\mu\epsilon}$, the impedance of free-space $\eta_0 = \sqrt{\mu_0/\epsilon_0} \approx 120\pi$ ohms, P_n^m are Associated Legendre functions of the first kind, $\hat{B}_n$ are Ricatti spherical Bessel functions, N_m is a truncation limit on the radial modal index n, and m is the azimuthal modal index. The modal coefficients a_{mn} and b_{mn} are determined to numerically enforce continuity of the fields via the moment method. While the previously mentioned form of the unimoment method (Morgan and Mei 1979) works well with nearly spherical objects, other three-dimensional orthogonal systems may be used for other shapes such as thin wires, where spherical harmonics are inefficient and converge slowly. In this case, the hemispherical mesh is very inefficient and comprises mainly free space. Objects such as the human body could be better modeled using spheroids and spheroidal harmonics.

Thus the finite element method employed was not without its complications. As stated, spherical harmonics were used to couple the exterior and interior (assumed) homogeneous regions. This resulted in huge computational overheads and increased errors for objects of large height-to-width ratios. Another problem was the evidence of large errors along the z-axis due to the use of derivative boundary conditions for the $m = 1$ mode along the z-axis and the fact that the high eccentricities of the whole-body resonance computations and large, complex propagation constants inside the body pushed the procedure and the computer upon which they were performed to the limit of its numerical precision and dynamic range. Hence only results for x- and y-axis internal fields were useful.

Similarly, the size of the computations in terms of the number of mesh points required for reasonable accuracy meant that run times were often more than 1,000 minutes. Optimized inversion techniques or the use of larger machines is required for further anatomical resolution using the axisymmetric CAP formulation.

Recently efforts have been made to extend the basic CAP formulation to more general three-dimensional geometries (Morgan 1990; Fleming 1990). Apart from the limitation of axisymmetry, one major drawback of the fourier modal analysis noted during the present extensive computations required by this paper was a need for special functions of very high order which demand high precision and large dynamic range. Efforts to generalize the formulation may utilize more primitive interpolants which should avoid such computational overheads.

■ ■